3D Hierarchically Structured CoS Nanosheets: Li^+ Storage Mechanism and Application of the High-Performance Lithium-ion Capacitors

Yun-Kai Wang[a], Mao-Cheng Liu[b], Jianyun Cao[c], Hu-Jun Zhang[a], Ling-Bin Kong* [a, b], David P. Trudgeon[d], Xiaohong Li[d], Frank C. Walsh[e]

[a] State Key Laboratory of Advanced Processing and Recycling of Non-ferrous Metals, Lanzhou University of Technology, Lanzhou 730050, China

[b] School of Materials Science and Engineering, Lanzhou University of Technology, Lanzhou 730050, China

[c] School of Materials, University of Manchester, Oxford Road, Manchester, M13 9PL, United Kingdom

[d] Renewable Energy Group, College of Engineering, Mathematics and Physical Sciences, University of Exeter, Penryn Campus, Cornwall TR10 9FE, United Kingdom

[e] Electrochemical Engineering Laboratory, National Centre for Advanced Tribology & Materials Engineering Research Group, University of Southampton, Highfield, Southampton, SO17 1BJ, United Kingdom

* Corresponding Author. Tel.: +86 (0)931 2976579; Fax: +86 (0)931 2976578; E-mail: konglb@lut.edu.cn

Abstract

Lithium-ion capacitors, which possess excellent power and energy densities, can combine both those advantages from supercapacitors and lithium-ion batteries, leading to the novel generation hybrid devices for storing energy. This study synthesized one three-dimensional (3D) hierarchical structure self-assembled from CoS nanosheets, according to a simple and efficient manner, have been used as anode for lithium ion capacitors. This CoS anode, based on a conversion-type Li^+ storage mechanism dominated by diffusion controlled, showed a large reversible capacity, together with excellent stability for cycling. The CoS shows a discharge capacity ≈ 434 mA h/g at 0.1 A/g. The hybrid lithium-ion capacitor, which had the CoS anode as well as the biochar cathode, exhibits excellent electrochemical performance with ultra-high energy and power densities of 125.2 Wh/kg and 6400 W/kg, respectively, and an extended cycling life of 81.75% retention after 40000 cycles. The CoS with self-assembled 3D hierarchical structure in combination with a carbon cathode offers a versatile device for future applications in energy storage.

Keywords

Self-assembled 3D hierarchical structure; Lithium-ion capacitors; Li^+ storage mechanism; High-performance; CoS, Metal Sulfide

Introduction

The efficient and versatile energy conversion and storage (ECS) has become a major endeavor of science and technology in recent years. From small portable energy storage equipment to large-scale power storage system, it is urgent to make the novel devices for storing energy that have considerable power and energy densities, as well as the extended cycling life. Electrochemical ECS devices arouse research interests as a result of the environmental acceptability, abundant resources of the active materials involved and reduced costs[1-3], in which, supercapacitors (SCs) and lithium-ion batteries (LIBs) are the primary devices that are under research, which is ascribed to the considerable power and energy densities.[4,5] SCs exhibits a great power density at 2-5 kW/kg, together with a perfect cycling life; However, practical application is limited by energy density. LIBs exhibit greater energy densities (ranging from 150 to 200 W h/kg), their cycling life and power densities are far inferior to those of SCs. [6-9] The metal ion hybrid capacitor is becoming a favored device as it combines the large power densities for SCs with excellent energy density from LIBs, thus it is highly expected as one of the most promising next generation ECS devices. [10-14]

Lithium-ion capacitors (LICs), which are constituted by the capacitive-type cathode and battery-type anode materials, together with the organic electrolytes, are first put forward in 2001.[15] The high energy density is ensured by the high cell voltage together with large specific capacity from reversible redox reaction (insertion, conversion, alloying) of lithium ions in the anode, meanwhile, the reversible anion (PF_6^-) desorption/adsorption on cathode surface achieves a high power density. This hybrid reaction mechanism is expected to fill the difference from LIBs to SCs on Ragone plot. [16-18] Various anode and cathode materials have been developed for LICs in the last decade and the upper limit of power-energy density for this technology has been advanced continuously. Throughout the existing LICs research reports, only at low power density can large energy density be shown, while the energy density significantly dropped at higher power density. [19-22] In consequence, further research and development of high performance LICs is important to ensure their future

applications practical circumstances.

Since the first report of LICs with a lithium titanate (LTO) and an activated carbon (AC) by Amatucci and colleagues,[15] diversed anode and cathode materials have been considered for LICs. [13,60] However, the entire LIC device has restricted electrochemical property, which may be related to imbalanced kinetics between adsorption/desorption and the faradic reaction that occurs on the cathode and the anode, respectively. [23,24] With regard to the mechanisms of reaction, LICs anode materials are classified as 3 types. The first type is based on the materials with the lithium insertion reaction mechanism, such as $LiCrTiO_4$,[25] $LiTi_2(PO_4)_3$, [26] TiP_2O_7, [27] $Li_2Ti_3O_7$,[28] and TiO_2 [29]. Although such materials have advantages of good structure stability and can exhibit excellent cycling performance, the high energy superiority of LICs cannot be obtained because the high de-intercalation potential limits the output voltage. The second category is based on the materials with the conversion reaction mechanism for lithium storage, such as Fe_2O_3,[30] V_2O_5,[31] VN,[32] MnO[33] and Nb_2O_5.[34] Materials with such mechanisms exhibit high capacity and good rate performance, but this conversion mechanism has large volume changes, leading to electrode polarization and capacity loss during long cycle periods. The third type is based on alloying reaction lithium storage mechanism, like the copper/silicon with dome pattern[35] as well as B-Si/SiO_2/C.[36] These materials can exhibit ultra-high capacity, but the large changes in volume accompanying those discharge and charge processes causes problems including sudden drop in capacity and shortened cycle life. Combining these issues, the conversion-type anode material has higher capacity characteristics than the insertion-type, and has a smaller volume expansion than the alloying type. Therefore, designing a structurally stable conversion type negative electrode will greatly improve cycle stability, thereby improving the device performance of LIC. In recent years, transition metal compound materials have rapidly become the focus of exploration as they have rich redox reaction valence state and good electron conductivity.[37-39, 63] Particularly, transition metal sulfide (TMSs), as a kind of electrochemical energy storage material with high theoretical capacity, has

attracted extensive attention.[40,61-62] However, TMSs show a limited performance as LIC electrode and there is considerable potential to develop improved electrode materials.

TMSs have abundance, reasonable cost, large theoretical capacity, structural diversity; as a result, great importance has been attached to them in the electrochemical energy storage field.[41] Such materials can be further divided into two types. The first type is TMSs have a layered structure, including MoS_2 [42], WS_2 [43] and TiS_2 [44]; The second type of TMSs has a non-layered structure which exhibits a high capacity due to the polyvalent redox site such as FeS_2.[45] Until now, TMSs that have been reported for use in LIBs and SCs include Co_9S_8 [46] and Ni_3S_2 [47]. In contrast, metal sulfides such as $CoNi_2S_4$ [48] $TiSe_{0.6}S_{1.4}$ [49] and TiS_2 [44] are poorly studied in the field of metal ion hybrid capacitors. Hence, exploration of these materials is of great significance for the advancement of LICs. On the other hand, the three-dimensional (3D) structure formed by the TMS nanosheets through physical and/or chemical interconnections inherits and optimizes the advantages of the 0D, 1D, or 2D nanostructures, while overcoming the volume change and capacity decay caused by the structural instability of the traditional TMSs.[50] Other than this, there are huge challenges involved in the synthesis of high-purity and well-defined 3D hierarchitectures by simple methods without any templates or surfactants. Future development of energy storage devices requires the design of three-dimensional, hierarchical TMSs, which could offer a superb platform to explore the energy storage mechanisms as well as the relationship between structure and performance.

This study used the hydrothermal approach for efficiently synthesizing the 3D hierarchical structure self-assembled of CoS nanosheets, as an anode material. It is demonstrated that the CoS anode of a conversion-type Li^+ reaction mechanism dominated by diffusion controlled has a high reversible charge capacity and excellent lithium storage stability; besides, when the specific current is 0.1 A/g, its capacity is as high as 434 mA h/g. (CoS//Carbon) LIC device constructed from the anode electrode (involving 3D hierarchical structure CoS) and the cathode (porous

structured biochar of Fructus Cannabis's Shells (FCS)) showed excellent power and energy densities at 6400 W/kg and 125.2 W h/kg, respectively, together with fascinating cycle performance, the retention rate can still reach 81.75% following 40,000 ultra-long discharge and charge cycles at 1 A/g.

Results and Conclusion

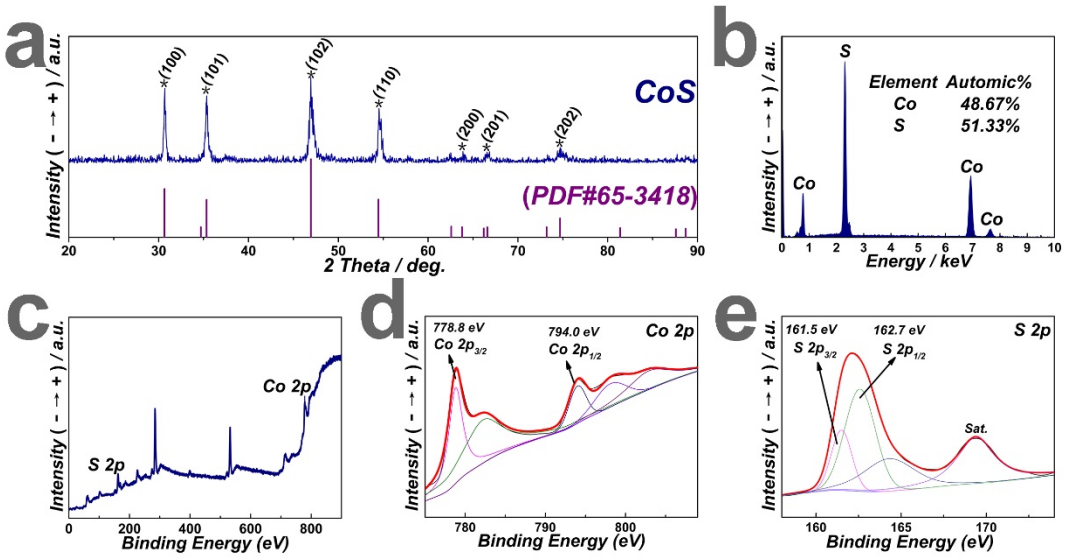

Figure 1 (a) XRD patterns for CoS, (b) EDS spectra for CoS, (c) XPS spectra (d) Co 2p (e) S 2p spectra for CoS.

Powder X-ray diffraction (XRD) was adopted to analyze crystal structures of that synthesized material. Fig.1a shows the typical XRD pattern of CoS for three-dimensional self-assembled nanosheet structure. As was observed, those diffraction peaks appearing at 2θ positions of 30.6°, 35.3°, 46.9°, 54.4°, 63.7°, 66.5°and 74.7° correspond to the (100), (101), (102), (110) (200), (201) and (202) crystal planes, respectively. All observable diffraction peaks matched very well to the standard X-ray diffraction mode of the hexagonal phase CoS (PDF No.65-3418), and no other characteristic peaks are detected, indicating that the obtained CoS product is a pure phase. In addition, very sharp and intense diffraction peaks indicate that the resulting product has high crystallinity. Energy dispersive spectroscopy (EDS) was carried out to determine the CoS composition. Our findings show that Co/S ratio in the sample was 48.67/51.33, and such figure was close to CoS stoichiometric ratio of

1/1 (Figure 1b). For more comprehensively exploring chemical composition and surface properties of CoS, X-ray photoelectron spectroscopy (XPS) was performed to determine samples. As suggested by those spectra acquired (Fig.1c), there were S and Co elements in the CoS sample. Figure 1d shows the Co 2p XPS spectra with high resolution, where peaks with binding energies of 798.8 eV and 794.0 eV are attributable to Co 2p1/2, whereas that at 803.9 eV was assigned to be the Co 2p1/2 satellite peak. The peaks at the 778.8 eV and 782.6 eV positions were attributed to Co 2p3/2 binding energy. The Co 2p3/2 peak appearing at the 778.8 eV position relates to the binding energy of cobalt-sulfide. The peaks exhibited by Co 2p1/2 and Co 2p3/2 in the Co 2p XPS spectrum confirm the formation of CoS. [51,52] In Figure 1e, S 2p XPS spectrum with high resolution shows two characteristic peaks at 162.7 and 161.5 eV, respectively, which were indexed to S 2p1/2 and S 2p3/2, respectively, while the peak at the 169.4 eV position is attributed to the surface sulfur in the high oxidation state. The peak with a binding energy of 164.3 eV represents Co-deficient, nonstoichiometric sulfides ($CoS_{1.097}$). [53] Co 2p and S 2p in the XPS spectrum have significant cobalt sulfide characteristics. The above results indicate that CoS with 3D hierarchical structure CoS has been successfully synthesized by a hydrothermal method.

Fig.2a, 2b and 2c show the CoS images obtained from scanning electron microscopy. Figure 2a shows that the CoS product consists of irregular three-dimensional particles resembling a walnut shape with several micrometers in diameter. Based on those SEM images with high resolution displayed within Figures 2b and 2c that the walnut shaped structure is assembled by interconnected hexagonal nanosheets with thickness from 10 to 100 nm. A single walnut shaped particle characterized by the interconnected thinner nanosheets embedded in the three-dimensional frame formed by thicker nanosheets. S1(Supporting Information) shows the specific formation mechanism. That self-assembled structure for interconnected nanosheets can effectively prevent the aggregation/restack of the nanosheets, can well buffer changes in volume caused by the discharge and charge

processes, ensure stability of the electrode material structure, and achieve stable capacity, and the existing pores between the intersecting nanosheets benefited electrolyte diffusion, together with the transport of lithium ions. Fig.2d displays the transmission electron microscopy (TEM) image, which conformed to results from Fig.2a, and that single microstructure shown on TEM images (Figure 2e and 2f) confirm the 3D walnut-like hierarchical nanostructures shown by SEM. High-resolution TEM images (Figure 2g) reveal a clear crystalline lattice with the spacings of 0.29 nm, which was indexed to (100) crystal planes at CoS phase of that hexagonal structure. Such result was supported by corresponding findings in the XRD analysis, and the successful synthesis of pure phase CoS with high crystallinity was proved. A STEM image, together with the related elemental mapping images for CoS (Figure 2i) demonstrates that the Co and S are uniformly distributed.

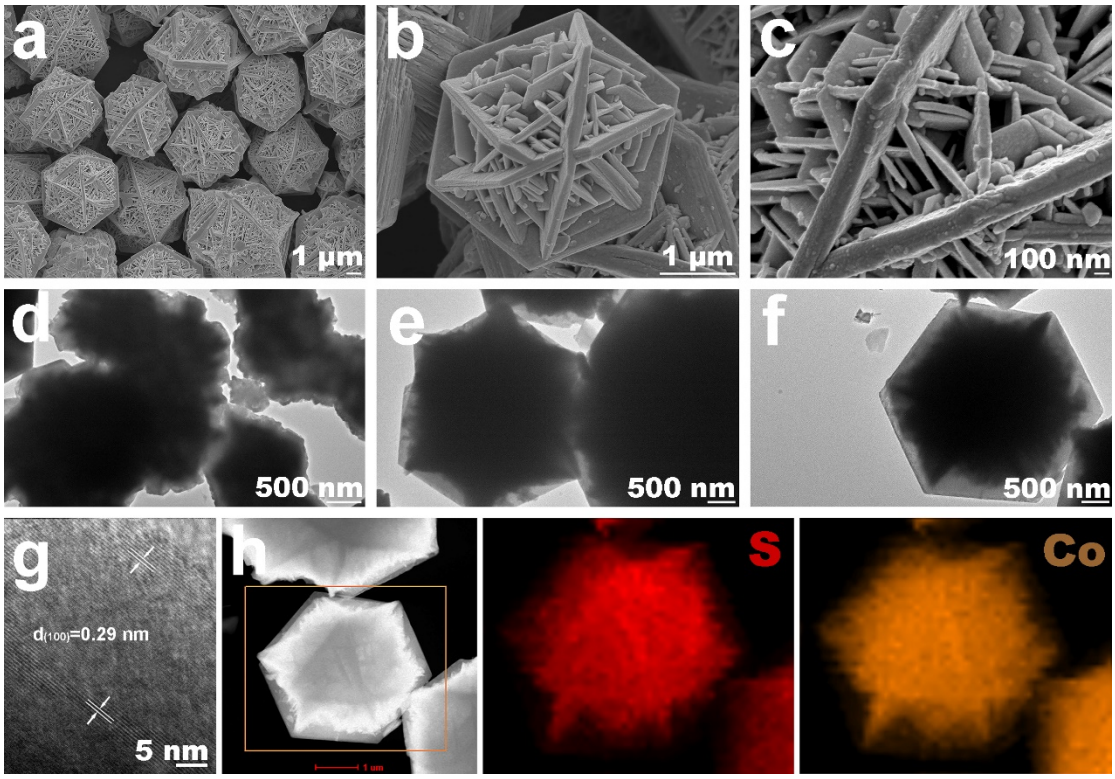

Figure 2 (a-c) SEM images for CoS, (d-f) TEM images for CoS, (g) HR-TEM image for CoS, (h) STEM image, together with the related elemental mapping images for CoS.

For studying that lithium storage mechanism and electrochemical properties of

CoS, electrochemical measurements were conducted using a half-cell setup consisting of a lithium foil (which was used to be the reference and electrode), and a CoS working electrode. Fig.3a displays those galvanostatic charge-discharge patterns for the CoS electrode when the specific current was 0.1 A/g. Typically, the first charge as well as discharge capacity was 498 and 596 mAh/g, respectively, while the platform presented at 1.45 V and 1.9 V in the curve may be related to reversible conversion reaction between CoS with Li: $CoS+2Li^{+}+2e^{-}\leftrightarrow Li_2S+Co$. [57-59,64] After the capacity remained stable, the shape and position of the platform remained essentially the same, indicating that CoS has a highly reversible conversion storage Li^{+} reaction. In order to verify the cycling stability of the material, SEM characterization was carried out on the samples after half battery cycling. (S2, Supporting Information) The charge-discharge curves are substantially identical after the fifth cycle, which is consistent with the results of cycling test as shown in Figure 3b. After the fifth cycle, capacity was still quite stable, with a coulombic efficiency of almost 100%, which had confirmed the electrode stability. That coulombic efficiency is below 100%, since a solid electrolyte mesophase is formed and there are irreversible side reactions; in addition, there is a small decrease in capacity during the first five cycles.[41] The reversible capacity of the CoS anode is 434 mAh/g when the specific current is 0.1 A/g.

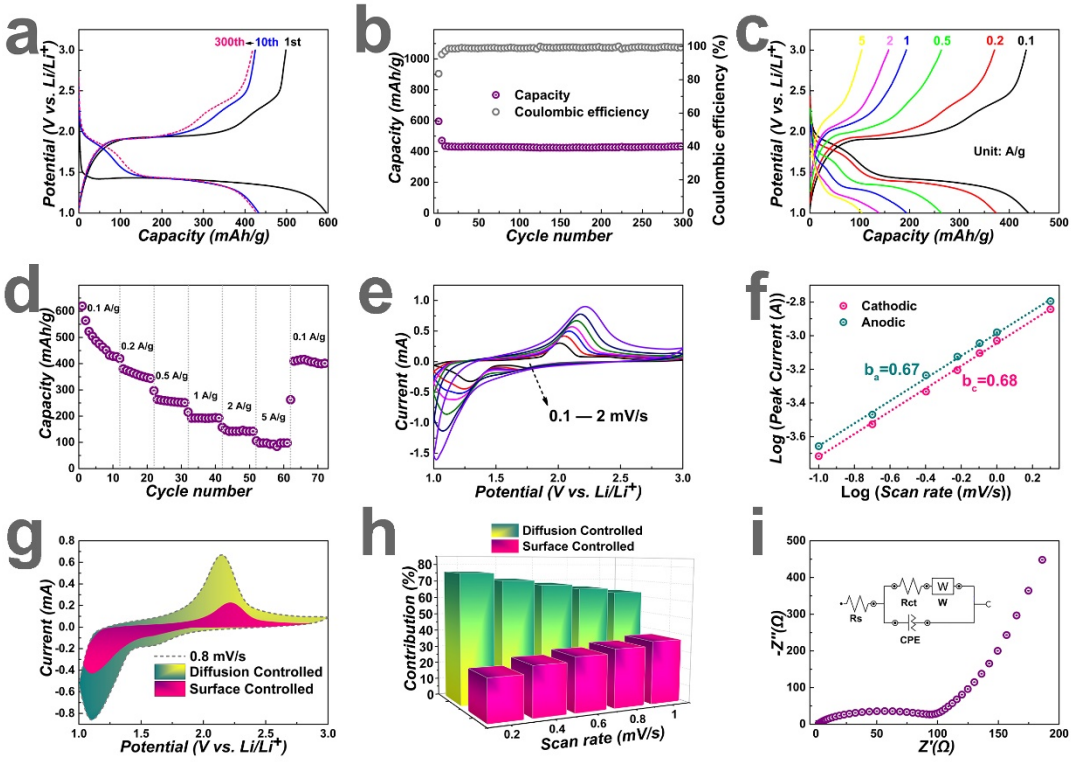

Figure 3 (a) Galvanostatic charge-discharge patterns for the CoS electrode when the specific current was 0.1 A/g, (b) Coulombic efficiency and cycle performance for the CoS electrode after 300 cycles when the specific current was 0.1 A/g, (c) Galvanostatic charge-discharge patterns for the CoS electrode under various specific currents, (d) Rate performance of CoS electrode under different rates (range, 0.1-5 A/g), (e) The CV curves obtained at different scanning rates (0.1-2 mV/s), (f) *b*-value determined based on the association of scanning rate with the peak current, (g) Contribution rate of two behaviors at 0.8 mV/s of the CoS electrode, (h) Contribution degree for the diffusion-controlled and capacitive charge versus the scanning rate, (i) Nyquist plots of CoS electrode, the inset is equivalent circuit model.

Additionally, those galvanostatic charge-discharge profiles under different current densities (Figure 3c) and the rate performance of CoS electrodes (Figure 3d) show that the specific capacity is 434, 371, 261, 192, 135 and 102 mAh/g when the specific currents were 0.1, 0.2, 0.5, 1, 2 and 5 A/g, separately. Such good rate performance and cycling stability are explained by that CoS 3D interconnected structure. That 3D interconnected structure assembled from CoS nanosheets is able to effectively buffer for changes in volume in the discharge-charge process, ensure stable output of the capacity, and this structure can facilitate the diffusion of electrolyte and the transportation of lithium ions, leading to excellent electrochemical performance.

In order to understand the lithium storage behavior of CoS anode, CV curves for CoS electrode under various scanning rates were plotted within the potential range of 1-3 V *vs.* Li/Li^+. As shown from Fig.3e, the enclosed area of CV curve gradually increases when the scanning rate is increased to 2 from 0.1 mV/s, while redox peak shape does not change significantly for all the CV curves, but the positions for reduction and oxidation peaks shifted to the low as well as high potential, separately. We think the reasons for this phenomenon are as follows: at low scan rates, the material as a whole has sufficient time to reach the equilibrium potential of the redox reaction. At high scanning rate, due to time limitation, lithium ion diffusion into bulk phase can hardly satisfy the balance of charge transfer, forcing the surface reaction to increase relatively, and the reaction of the electrode material is delayed, resulting in an increase in the over-potential of the reduction peak and the oxidation peak. In other words, the lithium ion diffusion rate cannot fully satisfy Li^+ consumption rate by the bulk reaction of the electrode, with the increase in scanning rate. Simultaneously, the enlargement of Potential increment in unit time shortens the reaction time of the electrode material, causing the lag of the electrochemical reaction, the peak shifts in a direction in which the over-potential increases. In order to confirm the above statement, the association of scanning rate with peak current has been further analyzed. It is generally considered that the values of scanning rate and peak current obey the power-law relationship: [54,55]

$$I = av^b \qquad (1)$$

$$\log (I) = b \log (v) + \log (a) \qquad (2)$$

in which I represents current, v stands for scanning rate; a as well as b in the equations represents the adjustable values. That value of b is evaluated by the slope in equation (2); specifically, the b value represents the electrochemical reaction under different behavioral controlled, $b = 0.5$ means a typical diffusion-controlled behavior, and $b = 1$ suggests completely surface-controlled contribution of the current. As shown in

Figure 3f, the log(v)-log(i) plots lead to the b values of 0.67 and 0.68 for the cathode and anode peaks, respectively. The b value is close to 0.5, indicating that both diffusion and surface controlled behaviors exist simultaneously, while the diffusion controlled current is the dominant one. For the purpose of further distinguishing the contribution of the two different behaviors, the current signal at a certain potential can be decoupled into diffusion controlled and surface controlled current by the equation: [56]

$$I(V)=k_1v+k_2v^{1/2} \quad (3)$$

in which k_1 as well as k_2 represents the determined values, v and I are the scan rate and current at a specific potential. While $k_2v^{1/2}$ and k_1v are diffusion-controlled and surface-controlled contributions, respectively. The surface-controlled region shown in Figure 3g indicates that 34.3% of the total charge when the scanning rate is 0.8 mV/s is surface-controlled. By using equation (3), the contribution of the two behaviors (diffusion-controlled *vs.* surface-controlled) are 75.8% *vs.*24.2%, 71.3% *vs.* 28.7%, 68.4% *vs.* 31.6%, 65.7% *vs.* 34.3% and 62.9% *vs.* 37.1% when the scanning rates are 0.2, 0.4, 0.6, 0.8 as well as 1 mV/s, separately (figure 3h). Results of kinetic analysis show that the charge storage of CoS electrode included diffusion controlled and surface controlled behaviors, in which diffusion controlled behavior dominates, therefore, most of the material's capacity is derived from the contribution of bulk reaction under diffusion control. With increase in the scanning rate, lithium ion diffusion rate cannot fully satisfy Li^+ consumption rate by the bulk reaction of the electrode. Meanwhile, the enlargement of potential increment in unit time shortens the reaction time of the electrode material, which leads to the proportion of bulk reaction is relatively reduced, while the proportion of active surface reaction is relatively increased. That is, when the scanning rate is increased, the proportion of the capacity contributed by diffusion controlled behavior is gradually decreased, and the proportion of the capacity contributed by surface reaction controlled behavior is gradually increased. Based on the above analysis, indicating that the charge storage of

CoS electrode involves a conversion-type mechanism dominated by diffusion controlled behavior of lithium ions inside the bulk CoS crystal. Impedance behavior of the CoS electrode is evaluated by electrochemical impedance spectroscopy (EIS) of with a half cell. Figure 4i displays Nyquist plots for CoS electrode in the frequency range of 0.1-100000 Hz. As was observed, those curves are constituted by one diagonal line and one semicircle within the low and high frequency regions, respectively. Typically, R_{ct} (charge transfer resistance), R_s (intrinsic impedance), W (Warburg Impedance) and *CPE* (constant phase element) are the components of that equivalent circuit model. Those fitted values of these components are shown in Table 1. The smaller R_s, R_{ct} and the Warburg impedance within that low frequency region associated with electron transfer and diffusion of lithium ions indicate an excellent electronic and ionic conductivity of the CoS electrode.

The SEM image shown in Figure 4a shows the FCS biochar materials has a coral-like morphology, with interconnected pores. To shed more light on the sample pore structure, we measure the sample nitrogen (N_2) desorption-adsorption isotherm curve. The N_2 desorption-adsorption isotherm curve shown in Fig.4b has a distinct hysteresis loop, indicating that the structure contains many micropores and a certain amount of macropores and mesopores, which is consistent with the results of the pore size distribution shown in Figure 4c. Moreover, the sample specific surface area is 1739.8 m^2/g by Brunauer-Emmett-Teller (BET) method from the gas desorption branch. It shows that the porous structure and ultra-large specific surface area of FCS contribute to the rapid PF_6^- ion diffusion and transportation within the electrolyte and the storage of surface charge.

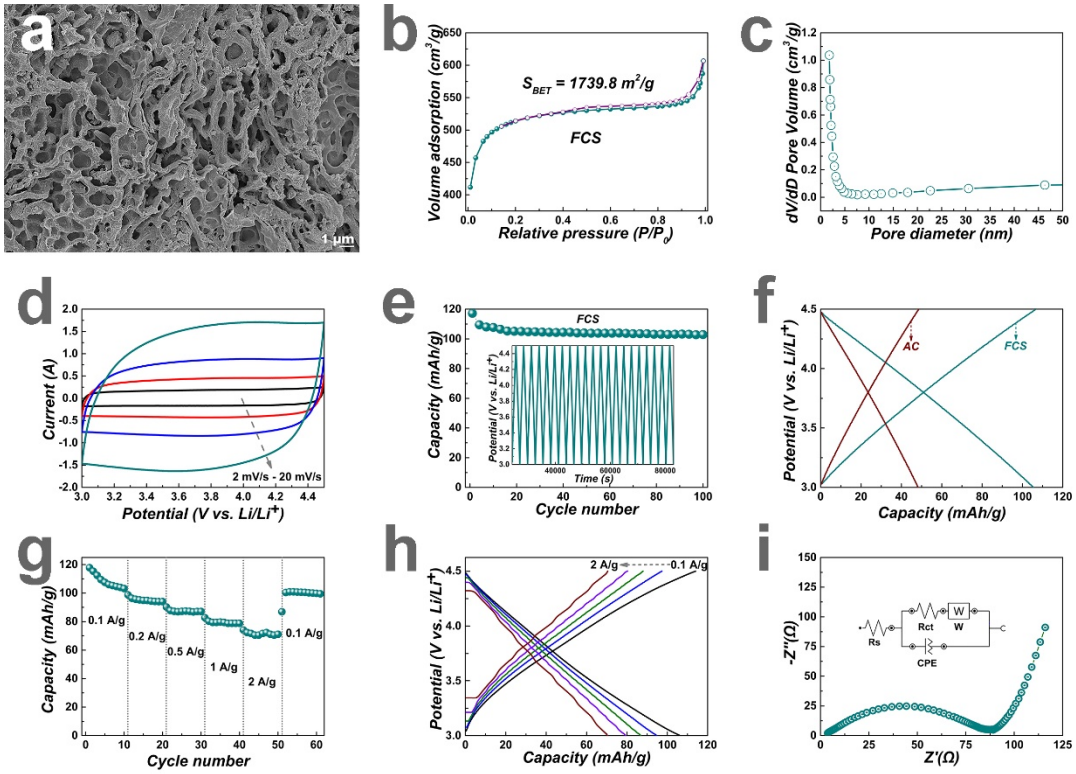

Figure 4 (a) SEM image for FCS, (b) N_2 desorption–adsorption isotherms, (c) Plots showing the distribution of pore size of FCS, (d) The CV curves of FCS under various scanning rates, (e) Cycle performance for FCS when the specific current was 0.1 A/g, (f) Galvanostatic charge-discharge profiles contrasts for FCS as well as AC under at 0.1 A/g, (g) Rate performance for FCS electrode, (h) galvanostatic charge-discharge patterns for the FCS electrode under various current densities, (i) Nyquist plots of FCS electrode, the inset is equivalent circuit model.

Under various scanning rates, those CV curves for the FCS electrodes show an almost ideal rectangular form which have no any oxidation-reduction peak within 3-4.5 V, which indicates that FCS electrodes exhibit a typical electric double layer capacitance (EDLC) behavior. (Figure 4d) Following constant current discharge-charge cycles for 100 times, the capacity of FCS is still 105 mAh/g when the specific current is 0.1 A/g, as suggested from Fig. 4e. According to Figure 4f, the specific capacity of FCS at the same specific current is twice that of commercial activated carbon (AC, 48 mAh/g). Furthermore, the results of the rate performance (Figure 4g) and those galvanostatic charge-discharge profiles under different current densities (Figure 4h) show that the specific capacities of the FCS cathode are 70 and

105 mAh/g when the specific currents are 2 and 0.1 A/g, respectively (the capacity retention is approximately 66%). Both of the rectangle shaped CV curves and the symmetrical linear shaped charge-discharge profiles indicate a typical EDLC behavior of the FCS cathode. The impedance behavior of the FCS electrode has been evaluated by EIS of a half cell, Figure 4i shows the Nyquist plots of FCS cathode with the frequency range of 0.1- 100000 Hz. There was one diagonal line and one semicircle within the low and high frequency regions of the curve. R_{ct} (charge transfer resistance), R_s (intrinsic impedance), W (Warburg Impedance), and CPE (constant phase element) are the components of that equivalent circuit model. The fitted component parameters are shown in Table 1. The slopes of the smaller *Rs*, *Rct* and the Warburg impedance in the low frequency region greater than 1 indicate the excellent electronic conductivity of the FCS electrode and the typical electric double layer capacitance behavior.

Combining the CoS anode with excellent lithium storage ability and the FCS cathode with ideal EDLC behavior, a novel LIC device has been constructed. As shown in Figure 5a, during charge and discharge, Lithium ion achieves charge storage by highly reversible conversion-type reaction in the CoS anode while PF_6^- is fleetly adsorbed/desorbed on the surface of the FCS cathode. Based on the potential window of the FCS cathode and the CoS anode, a cell voltage (range, 1.0-4.2 V) is selected for evaluating electrochemical properties for the whole device. Fig.5b suggests that, those CV curves for the LIC (CoS//FCS) demonstrate a quasi-rectangular shape at scanning rates of 2-20 mV/s, suggesting the different charge storage mechanisms for the cathode and anode electrodes are well matched and coordinated. Moreover, the galvanostatic charge-discharge profiles (Figure 5c) with a nearly symmetric and triangular shape confirm that, various mechanisms for the storage of charge are combined within that hybrid CoS//FCS LIC device.

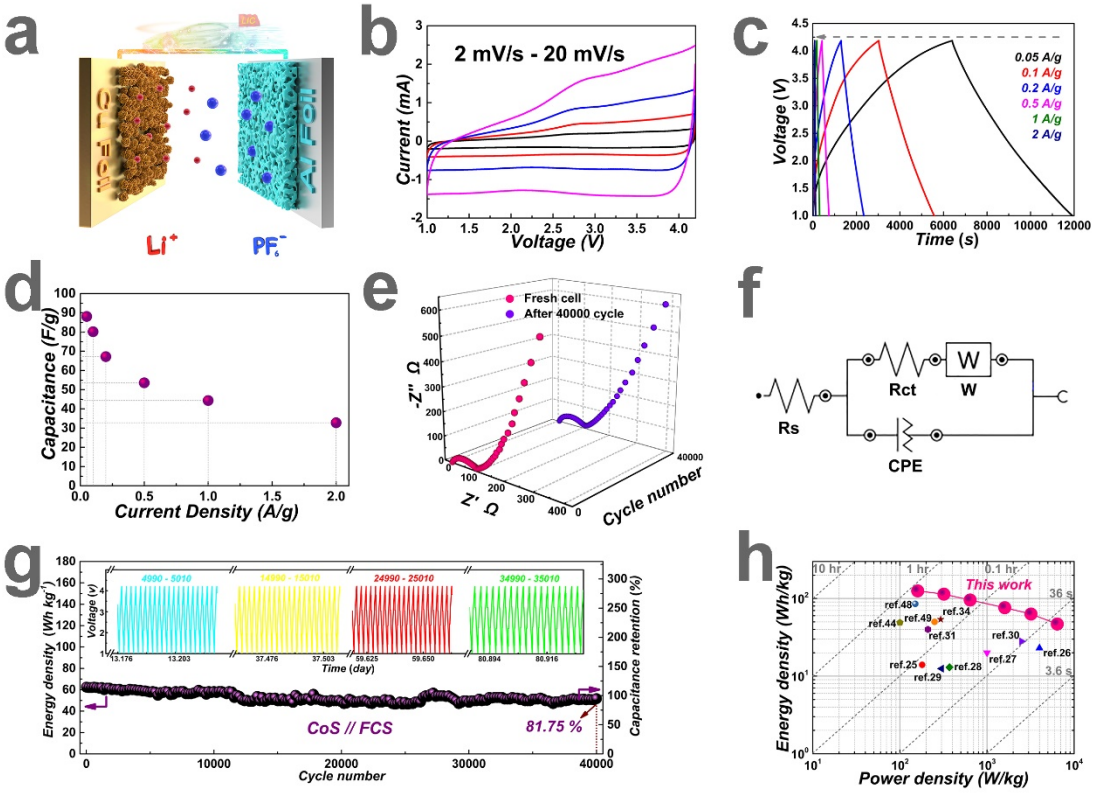

Figure 5 (a) Schematic diagram for LIC on the basis of CoS electrode and FCS electrode, (b) The CV curves for CoS//FCS under different scanning rates (range, 2-20 mV/s), (c) Rate performance of CoS//FCS LIC under various densities of current, (d) The galvanostatic discharge-charge curves for CoS//FCS LIC under various densities of current, (e) electrochemical impedance spectra of CoS//FCS LIC recorded as fresh cell and after 40000 cycles, (f) equivalent circuit model of CoS//FCS LIC, (g) Cycling performance of CoS//FCS LIC, (h) The Ragone plots for CoS//FCS LIC, and those scattered points were consistent with LICs data obtained based on related literature.

The device specific capacitance is computed as follows:

$$C = I \cdot t / m \cdot \Delta V \qquad (4)$$

in which ΔV represents voltage difference, I stands for current, m suggests mass of the CoS and FCS, and t indicates discharge time. As shown in Figure 5d, the device specific capacitances are 88.1, 80.2, 67.2, 53.6, 44.4 as well as 32.8 F/g at 0.05, 0.1, 0.2, 0.5, 1 as well as 2 A/g, separately. Fig.5e displays the Nyquist plots for LIC at the frequency range of 0.1-100000 Hz. There was one diagonal line and one semicircle

within the low and high frequency regions of the curve. R_{ct} (charge transfer resistance), R_s (intrinsic impedance), W (Warburg Impedance), and CPE (constant phase element) are the components of that equivalent circuit model, (Fig.5f) Table 1 shows the fitted component parameters. (Impedance fitting details are shown in S3) After 40,000 cycles, the variation of R_s and R_{ct} and Warburg impedance is particularly small, indicating that the CoS//FCS device has excellent cycling stability.

As shown in Figure 5h, the Ragone plots exhibit the association of power density with energy density for the CoS//FCS LIC. The device power and energy densities are computed according to the equations below:

$$E=1/2 \cdot C \cdot (\Delta V)^2 \quad (5)$$

$$P=E/t \quad (6)$$

$$\Delta V=V_{max}-V_{min} \quad (7)$$

in which V_{min} and V_{max} represent the minimum and maximum voltage values in the process of discharge, C is the capacitance normalized to total active material mass for two electrodes, whereas t stands for the duration of discharge. When the energy density is, The power density of CoS//FCS LIC device is 160 W/kg when energy density is 125.2 Wh/kg; besides, energy density for the device remains at 60.8 Wh/kg when the power density is 6400 W/kg. In addition, that device has a superb cycle stability. In Fig.5g, that device capacitance retention is 81.75% after cycling 40,000 for times when the current density is 1 A/g, and such cycling stability can be comparable to that of an EDLC capacitor.

This device excellent energy storage capacity is attributed to several aspects below: i) device design by selection of the anode electrode (CoS) and cathode electrode (FCS porous carbon); ii) good structural properties inherent in the electrode material and excellent electrochemical performance of individual anode and cathode

material; iii) Reasonable matching of the hybrid device enables mutual coordination of the different reaction mechanisms. Compared to the performance of literature reported LICs (Table 2), the exhibits outstanding electrochemical performance, suggesting great prospects and potential of the hybrid device. The prepared hybrid CoS//FCS LIC has excellent energy and power densities, together with superb long-term cycle stability, which is attractive in the field of energy storage in the future.

Conclusions

To sum up, CoS with a 3D hierarchical structure is synthesized according to a simple while efficient approach. The CoS anode based on the conversion-type Li^+ storage mechanism dominated by diffusion controlled has high reversible capacity, excellent lithium storage stability, and its capacity is about 434 mA h/g when the specific current is 0.1 A/g. In addition, that LIC device constructed in combination with the biochar cathode exhibits excellent electrochemical performance and exerts an ultra-large energy and power densities of 6400 W/kg 125.2 Wh/kg, respectively, together with extremely long-term cycling life of 81.75% after 40000 cycles. This paper is the first to report the application of the CoS anode material with 3D hierarchical structure in lithium ion energy storage. It demonstrates the applicability of CoS anode material for hybrid capacitors and reveals the lithium storage mechanism. The excellent prospects and development potential in the future energy storage field of (CoS//FCS) LIC device are confirmed by excellent electrochemical performance which lays a foundation for the application of the three-dimensional structure TMS material energy storage device.

Experimental Section

Synthesis of CoS

The chemicals used in this work are of analytical grade and are used as received.

Cobalt (II) chloride hexahydrate (99%, AR) as well as thiourea (99%, AR) was purchased from Sinopharm Chemical reagent Co., Ltd. A hydrothermal synthesis method was adopted. Typically, 140 ml of deionized water was used to dissolve 3.57 g cobalt chloride hexahydrate under 50 °C for 30 minutes, followed by the addition of 6.09 g thiourea in the solution mentioned above; thereafter, the solution mixture was subjected to vigorous stirring for 30 minutes under 50 °C. Thereafter, the resultant mixture would be transferred to the 200 mL Teflon-lined stainless-steel autoclave followed by 750 min of maintenance under 200 °C. Later, that autoclave would be taken out to cool until ambient temperature. Subsequently, the resultant black precipitate would be extracted through centrifugation, repeatedly rinsed by deionized water and ethanol, and dried for 12 h within the vacuum oven under 60 °C.

Preparation of Porous Carbon

The FCS, obtained by peeling off from the purchased Fructus Cannabis, was washed with alcohol as well as deionized water, followed by overnight drying under the temperature of 80 °C. Then, FCS would be pre-carbonized within the muffle furnace for 3 h under the temperature 300 °C. The pre-carbonized FCS and KOH with a mass ratio of 1:1 are dispersed/dissolved in water and stirred vigorously for 4 h. Thereafter, the resultant mixture would be dried for a period of 12 h within the vacuum oven, and then maintained for 2 h under 700 °C within a tube furnace under N_2 atmosphere. Then the product was naturally cooled down until ambient temperature, followed by repeated washing by deionized water as well as 1 mol/L HCl aqueous solution. Eventually, that sample would be dried within the vacuum oven for 12 h under the temperature of 80 °C.

Characterization of Materials

X-Ray Diffraction (XRD, Rigaku, D/MAX 2400, Japan) was adopted to determine the CoS crystal structures, and its 2theta was 20°-90°. Elemental composition as well as

valence of CoS was identified through X-ray photoelectron spectroscopy (XPS, ESCALAB 250xi). Afterwards, distribution of pore size and specific surface for FCS was analyzed using Brunauer−Emmett−Teller (BET, JW-BK200C). Sample elemental content was evaluated through energy dispersive spectroscopy (EDS). Furthermore, transmission electron microscopy (TEM, JEOL, JEM-2010, Japan) and scanning electron microscopy (SEM, JEOL, JSM-6701F, Japan) are employed to record the microstructure and morphology of CoS.

Preparation of Electrodes and Assembly of Button cells

CoS and FCS electrodes were prepared by slurry coating. Typically, active material (70 mg), conductive additive (acetylene black, 15 mg) as well as binder (sodium alginate, 15 mg) was dispersed into the deionized water (1 mL), followed by 12 h of stirring for forming the uniform slurry. Subsequently, that slurry would be applied evenly onto the clean aluminum/copper foil collector using a coating device. The coted foil was subjected to 12 h of drying within the oven under 60 °C, followed by punching into disc electrodes with an area of 1.33 cm^2. These electrodes were further dried in a vacuum oven for 12 hours, and then put into the glove box for further use. The active material loading masses are 2.4-4 and 0.6-0.8 mg in cathode and anode separately. All button cells (battery model: LIR 3032) are packaged into the glove box filled with argon, the water and oxygen content are <0.01 ppm. Specifically, the electrolyte and separator used were 1 mol/L $LiPF_6$ contained within the (EC/DEC/EMC,1:1:1) and Celgard 2400, respectively. Metal lithium (reference and counter electrode) and working electrode (CoS or FCS) are assembled in a half-cell configuration. The active material masses in cathode and anode within the entire battery are determined according to the charge conservation formula $(C \cdot V \cdot M)_{anode} = (C \cdot V \cdot M)_{cathode}$, and the active material ratio of the anode to cathode is 1:5. A pre-lithiated CoS electrode (discharged to 1 V after ten cycles) is assembled with a pre-activated FCS cathode (charged to 4.2 V after ten cycles) as a full cell.

Electrochemical measurements

The charge-discharge and cycle performance were analyzed by LAND (CT-2001A) battery test system, and all electrochemical assays were carried out under ambient temperature. The charge-discharge and CV curves were obtained using electrochemical impedance spectroscopy (EIS) and the Electrochemical Workstation (CHI660D, Shanghai, China); in addition, the Metrohm Autolab (PGSTAT 128N) Electrochemical Workstation (Metrohm China Co., Ltd.) was adopted to obtain the equivalent circuit model (software utilized for model acquisition and modeling was added).

Assoclated Content

Supporting Information available: [the specific formation mechanism of 3D Hierarchically Structured CoS Nanosheets; SEM characterization of 3D Hierarchically Structured CoS Nanosheets after cycling; Impedance fitting details of CoS//FCS LIC device]

Acknowledgments

This work was supported by the National Natural Science Foundation of China (No. 51971104, 51762031).

References

(1) Armand, M.; Tarascon, J.-M. Building Better Batteries. Nature, 2008, 451(7179), 652−657.

(2) Wang, F.; Wu, X.; Yuan, X.; Liu, Z.; Zhang, Y.; Fu, L.; Huang, W. Latest Advances in Supercapacitors: From New Electrode Materials to Novel Device Designs. Chemical Society Reviews 2017, 46(22), 6816-6854.

(3) Hwang, J. Y.; Myung, S. T.; Sun, Y. K. Sodium-ion Batteries: Present and Future. Chemical Society Reviews 2017, 46, 3529-3614.

(4) Augustyn, V.; Simon, P.; Dunn, B. Pseudocapacitive Oxide Materials for Highrate Electrochemical Energy Storage. Energy & Environmental Science 2014, 7(5), 1597 –1614.

(5) Dubal, D. P.; Ayyad, O.; Ruiz, V.; Gómez-Romero, P. Hybrid Energy Storage: the Merging of Battery and Supercapacitor Chemistries. Chemical Society Reviews 2015, 44’(7), 1777−1790.

(6) Zhang, W.-B.; Ma, X.-J.; Kong, L.-B. Nanocrystalline Intermetallic Tungsten Carbide: Nanoscaled Solidoid Synthesis, Nonfaradaic Pseudocapacitive Property, and Electrode Material Application. Advanced Materials Interfaces 2017, 4(13), 1700099.

(7) Gu, H.; Zhu, Y.-E.; Yang, J.; Wei, J.; Zhou, Z. Nanomaterials and Technologies for Lithium-ion Hybrid Supercapacitors. ChemNanoMat 2016, 2(7), 578−587.

(8) Ma, Y.; Chang, H.; Zhang, M.; Chen, Y. Graphene-based Materials for Lithium-ion Hybrid Supercapacitors. Advanced Materials 2015, 27(36), 5296−5308.

(9) Li, B.; Dai, F.; Xiao, Q.; Yang, L.; Shen, J.; Zhang, C.; Cai, M. Activated Carbon from Biomass Transfer for High-Energy Density Lithium-ion Supercapacitors. Advanced Energy Materials 2016, 6(18), 1600802.

(10) Gogotsi, Y.; Penner, R. M. Energy Storage in Nanomaterials–capacitive,

Pseudocapacitive, or Battery-like?. ACS Nano 2018, 12, 2081−2083.

(11) Xu, H.; Hu, X.; Sun, Y.; Luo, W.; Chen, C.; Liu, Y.; Huang, Y. Highly Porous Li4Ti5O12/C Nanofibers for Ultrafast Electrochemical Energy Storage. Nano Energy 2014, 10, 163-171.

(12) Won, J. H.; Jeong,H.; M. Kang, J. K. Synthesis of Nitrogen-richnanotubes with Internal Compartments having Open Mesoporous Channels and Utilization to Hybrid Full-cell Capacitors Enabling High Energy and Power Densities over Robust Cycle Life. Advanced Energy Materials 2017, 7(1), 1601355.

(13) Wang, H.; Zhu, C.; Chao, D.; Yan, Q.; Fan, H. J. Nonaqueous Hybrid Lithium-ion and Sodium-ion Capacitors. Advanced Materials 2017, 29(46), 1702093.

(14) Jeżowski, P.; Crosnier, O.; Deunf, E.; Poizot, P.; Béguin, F.; Brousse, T. Safe and Recyclable Lithium-ion Capacitors Using Sacrificial Organic Lithium Salt. Nature materials 2018, 17(2), 167-173.

(15) Amatucci, G. G.; Badway, F.; Du Pasquier, A.; Zheng, T. An Asymmetric Hybrid Nonaqueous Energy Storage Cell. Journal of The Electrochemical Society 2001, 148(8), A930−A939.

(16) Hall, P. J.; Mirzaeian, M.; Fletcher, S. I.; Sillars, F. B.; Rennie, A. J. R.; Shitta-Bey, G. O.; Wilson, G.; Cruden, A. Energy Storage in Electrochemical Capacitors: Designing Functional Materials to Improve Performance. Energy & Environmental Science 2010, 3(9), 1238−1251.

(17) Simon, P.; Gogotsi, Y. Materials for Electrochemical Capacitors. Nature Materials 2008, 7, 845−854.

(18) Amaresh, S.; Karthikeyan, K.; Jang, I.-C.; Lee, Y. S. Single-step Microwave Mediated Synthesis of the Cos2 Anode Material for High Rate Hybrid Supercapacitors. Journal of Materials Chemistry A 2014, 2(29), 11099−11106.

(19) Song, Z.; Zhou, H. Towards Sustainable and Versatile Energy Storage Devices: An Overview Of Organic Electrode Materials. Energy & Environmental Science 2013, 6(8), 2280-2301.

(20) Wang, S.; Wang, L.; Zhang, K.; Zhu, Z.; Tao, Z.; & Chen, J. Organic Li4C8H2O6 Nanosheets for Lithium-Ion Batteries. Nano letters 2013, 13(9), 4404-4409.

(21) Lee, M.; Hong, J.; Kim, H.; Lim, H. D.; Cho, S. B.; Kang, K.; Park, C. B. Organic Nanohybrids for Fast and Sustainable Energy Storage. Advanced Materials 2014, 26(16), 2558-2565.

(22) Hu, Z.; Sayed, S.; Jiang, T.; Zhu, X.; Lu, C.; Wang, G.; Liu, Z. Self-assembled Binary Organic Granules with Multiple Lithium Uptake Mechanisms toward High-Energy Flexible Lithium-Ion Hybrid Supercapacitors. Advanced Energy Materials 2018, 8(30), 1802273.

(23) Reddy, M. V.; Subba Rao, G. V.; Chowdari, B. V. R. Metal Oxides and Oxysalts as Anode Materials for Li ion Batteries. Chemical Reviews 2013, 113(7), 5364-5457

(24) Shen, L.; Lv, H.; Chen, S.; Kopold, P.; van Aken, P. A.; Wu, X.; Yu, Y. (). Peapod-like Li3VO4/N-doped Carbon Nanowires with Pseudocapacitive Properties as Advanced Materials for High-Energy Lithium-ion Capacitors. Advanced Materials 2017, 29(27), 1700142.

(25) Aravindan, V.; Chuiling, W.; Madhavi, S. High Power Lithium ion Hybrid Electrochemical Capacitors using Spinel Licrtio4 as Insertion Electrode. Journal of Materials Chemistry A 2012, 22(31), 16026−16031.

(26) Aravindan, V.; Chuiling, W.; Reddy, M. V.; Rao, G. V. S.; Chowdari, B. V. R.; Madhavi, S. Carbon Coated Nano-Liti2(PO4)3 Electrodes for Non-aqueous Hybrid Supercapacitors. Physical Chemistry Chemical Physics 2012, 14(16), 5808−5814.

(27) Aravindan, V.; Reddy, M. V.; Madhavi, S.; Mhaisalkar, S. G.; Subba Rao, G. V.; Chowdari, B. V. R. Hybrid Supercapacitor with Nano-Tip2o7 as Intercalation Electrode. Journal of Power Sources 2011, 196(20), 8850−8854.

(28) Chen, F.; Li, R.; Hou, M.; Liu, L.; Wang, R.; Deng, Z. Preparation and Characterization of Ramsdellite Li2Ti3O7 as an Anode Material for Asymmetric Supercapacitors. Electrochim. Acta 2005, 51(1), 61−65.

(29) Gao, L.; Huang, D.; Shen, Y.; Wang, M. Rutile-TiO2 decorated Li4Ti5O12 Nanosheet Arrays with 3D Interconnected Architecture as Anodes for High Performance Hybrid Supercapacitors. Journal of Materials Chemistry A 2015, 3(46), 23570-23576.

(30) Karthikeyan, K.; Amaresh, S.; Lee, S. N.; Aravindan, V.; Lee, Y. S. Fluorine-doped Fe2O3 as High Energy Density Electroactive Material for Hybrid Supercapacitor Applications. Chemistry–An Asian Journal 2014, 9(3), 852-857.

(31) Chen, Z.; Augustyn, V.; Wen, J.; Zhang, Y.; Shen, M.; Dunn, B.; Lu, Y. High-performance Supercapacitors Based on Intertwined CNT/V2O5 Nanowire Nanocomposites. Advanced Materials 2011, 23(6): 791-795.

(32) Lu, X.; Liu, T.; Zhai, T.; Wang, G.; Yu, M.; Xie, S.; Ling, Y.; Yu, H.; Tong, Y.; Li, Y. Improving the Cycling Stability of Metal–nitride Supercapacitor Electrodes with a Thin Carbon Shell. Advanced Energy Materials 2014, 4(4), 1300994.

(33) Chen, K.; Zhang, F.; Sun, J.; Li, Z.; Zhang, L.; Bachmatiuk, A.; Zou, Z.; Zhang, L.; Rummeli, H.; Liu, F.; Liu, Z. (). Growth of Defect-engineered Graphene on Manganese Oxides for Li-Ion Storage. Energy Storage Materials 2018,12, 110-118.

(34) Sun, H.; Mei, L.; Liang, J.; Zhao, Z.; Lee, C.; Fei, H.; Ding, M.; Lau, J.; Li, M.; Wang, C.; Xu, X. Three-dimensional Holey-graphene/niobia Composite

Architectures for Ultrahigh-rate Energy Storage. Science 2017, 356(6338), 599-604.

(35) Liu, X.; Jung, H.-G.; Kim, S.-O.; Choi, H.-S.; Lee, S.; Moon, J. H.; Lee, J. K. Silicon/Copper Dome-patterned Electrodes for Highperformance Hybrid Supercapacitors. Scientific reports 2013, 3, 3183.

(36) Yi, R.; Chen, S.; Song, J.; Gordin, M. L.; Manivannan, A.; Wang, D. High-performance Hybrid Supercapacitor Enabled by a High-Rate Si-based Anode. Advanced Functional Materials 2014, 24(47), 7433−7439.

(37) Xiao, X.; Song, H.; Lin, S.; Zhou, Y.; Zhan, X.; Hu, Z.; Jiao, L. Scalable Salt-templated Synthesis of Two-dimensional Transition Metal Oxides. Nature communications 2016, 7, 11296.

(38) Hu, Z.; Xiao, X.; Jin, H.; Li, T.; Chen, M.; Liang, Z.; J, Guo.; J, Li.; L, Wan, Huang.; Zhang, Y. Rapid Mass Production of Two-Dimensional Metal Oxides and Hydroxides Via the Molten Salts Method. Nature communications 2017, 8, 15630.

(39) Lan, D.; Chen, Y.; Chen, P.; Chen, X.; Wu, X.; Pu, X.; Zeng, Y.; Zhu, Z. Mesoporous Coo Nanocubes@ Continuous 3D Porous Carbon Skeleton of Rose-based Electrode for High-Performance Supercapacitor. ACS applied materials & interfaces 2014, 6(15), 11839-11845.

(40) Geng, P.; Zheng, S.; Tang, H.; Zhu, R., Zhang, L.; Cao, S., C, Shuai.; X, Huaiguo.; Pang, H. Transition Metal Sulfides Based on Graphene for Electrochemical Energy Storage. Advanced Energy Materials 2018, 8(15), 1703259.

(41) Liu, Y.; Li, Y.; Kang, H.; Jin, T.; Jiao, L. Design, Synthesis, and Energy-related Applications of Metal Sulfides. Materials Horizons 2016, 3(5), 402-421.

(42) Chang, K.; Chen, W. In Situ Synthesis Of Mos2/Graphene Nanosheet Composites with Extraordinarily High Electrochemical Performance for

Lithium ion Batteries. Chemical Communications 2011, 47(14), 4252–4254.

(43) Liu, Y.; Wang, W.; Wang, Y.; Peng, X. Homogeneously Assembling Like-Charged WS2 and GO Nanosheets Lamellar Composite Films by Filtration for Highly Efficient Lithium ion Batteries. Nano Energy 2014, 7, 25-32.

(44) Chaturvedi, A.; Hu, P.; Aravindan, V.; Kloc, C.; Madhavi, S. Unveiling Two-dimensional Tis2 as an Insertion Host for the Construction of High Energy Li-Ion Capacitors. Journal of Materials Chemistry A 2017, 5(19), 9177−9181.

(45) Fong, R.; Dahn, J. R.; Jones, C. H. W. Electrochemistry of Pyrite-based Cathodes for Ambient Temperature Lithium Batteries. Journal of The Electrochemical Society 1989,136(11), 3206-3210.

(46) Luo, W.; Xie, Y.; Wu, C.; Zheng, F. Spherical Cos2@Carbon Core-shell Nanoparticles: One-pot Synthesis and Li Storage Property. Nanotechnology 2008, 19(7), 075602.

(47) Yu, W.; Lin, W.; Shao, X.; Hu, Z.; Li, R.; Yuan, D. High Performance Supercapacitor Based on Ni3S2/Carbon Nanofibers and Carbon Nanofibers Electrodes Derived from Bacterial Cellulose. Journal of Power Sources 2014, 272, 137−143.

(48) Jagadale, A.; Zhou, X.; Blaisdell, D.; Yang, S. Carbon Nanofibers (Cnfs) Supported Cobalt-Nickel Sulfide (Coni2s4) Nanoparticles Hybrid Anode for High Performance Lithium ion Capacitor. Scientific reports 2018, 8(1), 1602-1613.

(49) Chaturvedi, A.; Hu, P.; Kloc, C.; Lee, Y. S.; Aravindan, V.; Madhavi, S. High Energy Li-Ion Capacitors Using Two-Dimensional Tise0.6S1.4 as Insertion Host. Journal of Materials Chemistry A .2017, 5(37), 19819-19825

(50) Xia, H.; Xu, Q.; Zhang, J. Recent Progress on Two-dimensional Nanoflake

Ensembles for Energy Storage Applications. Nano-micro letters 2018, 10, 66-96.

(51) Yuan, H.; Liu, J.; Li, H.; Su, K.; Liu, X.; Li, Y.; Q, Shi.; Y, Wu.; Zhao, Jiao, Q. Rational Integration of Hierarchical Structural Cos1.097 Nanosheets/Reduced Graphene Oxide Nanocomposites with Enhanced Electrocatalytic Performance for Triiodide Reduction. Carbon 2018, 126, 514-521.

(52) Jiang, D.; Liang, H.; Liu, Y.; Zheng, Y.; Li, C.; Yang, W.; Yang, W.; Liu, J.; Barrow, C, J. In Situ Generation of Cos1.097 Nanoparticles on S/N Co-doped Graphene/Carbonized Foam for Mechanically tough and Flexible All Solid-State Supercapacitors. Journal of Materials Chemistry A, 2018, 6(25): 11966-11977

(53) Chen, H.; Zhu, X.; Chang, Y.; Cai, J.; Zhao, R. 3D Flower-like Cos Hierarchitectures Recycled from Spent Licoo2 Batteries and Its Application in Electrochemical Capacitor. Materials Letters 2018, 218, 40-43.

(54) Wang, J.; Polleux, J.; Lim, J.; Dunn, B. Pseudocapacitive Contributions to Electrochemical Energy Storage in Tio2 (Anatase) Nanoparticles. The Journal of Physical Chemistry C 2007, 111(40), 14925−14931.

(55) Augustyn, V.; Simon, P.; Dunn, B. Pseudocapacitive Oxide Materials for High-rate Electrochemical Energy Storage. Energy & Environmental Science 2014, 7(5), 1597-1614.

(56) Augustyn, V.; Come, J.; Lowe, M. A.; Kim, J. W.; Taberna, P. L.; Tolbert, S. H.; Abruna, H. D.; Simon, P.; Dunn, B. High-rate Electrochemical Energy Storage Through Li+ Intercalation Pseudocapacitance. Nature materials 2013, 12, 518-522.

(57) Wang, H.; Ma, J.; Liu, S.; Nie, L.; Chai, Y.; Yang, X.; Yuan, R. Cos/Cnts Hybrid Structure for Improved Performance Lithium Ion Battery. Journal of Alloys and Compounds, 2016, 676, 551-556.

(58) Kim, Y.; Goodenough, J. B. Lithium Insertion into Transition-metal Monosulfides: Tuning the Position of the Metal 4s Band. The Journal of Physical Chemistry C, 2008, 112(38), 15060-15064.

(59) Wang, Q.; Jiao, L.; Du, H.; Peng, W.; Han, Y.; Song, D.; Yuan, H. Novel Flower-like Cos Hierarchitectures: One-pot Synthesis and Electrochemical Properties. Journal of Materials Chemistry, 2011,21(2), 327-329.

(60) Lang, J.; Zhang, X.; Yang, B.; Li, H.; Yan, X. Research Progress in Nonaqueous Lithium/Sodium-Ion Capacitors. SCIENTIA SINICA Chimica, 2018, 48(12), 1478-1513.

(61) Wei, X.; Tan, X.; Meng, J.; Wang, X.; Hu, P.; Yang, W.; Mai, L. Amine-assisted Synthesis of FeS@ NC Porous Nanowires for Highly Reversible Lithium Storage. Nano Research, 2018, 11(12), 6206-6216.

(62) Zhang, L.; Sun, D.; Wei, Q.; Ju, H.; Feng, J.; Zhu, J.; Guo, J. Understanding the Electrochemical Reaction Mechanism of VS2 Nanosheets in Lithium-ion Cells by Multiple in Situ and ex Situ X-ray Spectroscopy. Journal of Physics D: Applied Physics, 2018, 51(49), 494001.

(63) Yuan, H.; Wu, M.; Zheng, J.; Chen, Z. G.; Zhang, W.; Luo, J.; Xia, Y. Empowering Metal Phosphides Anode with Catalytic Attribute toward Superior Cyclability for Lithium-Ion Storage. Advanced Functional Materials, 2019, 29(17), 1809051.

(64) Yang, T.; Yang, D.; Liu, Y.; Liu, J.; Chen, Y.; Bao, L.; Ling, C. D. MOF-derived carbon-encapsulated cobalt sulfides orostachys-like micro/nano-structures as advanced anode material for lithium ion batteries. Electrochimica Acta, 2018, 290, 193-202.

Tables and Captions

Table 1. Fitted EIS parameters obtained from CoS electrode, FCS electrode and LIC (CoS//FCS).

Sample	CoS electrode	FCS electrode	CoS//FCS fresh	CoS//FCS 40000 cycles
R_s (Ω)	1.6	3.6	3.4	4.9
R_{ct} (Ω)	112.7	97.3	102.5	91.8

Table 2. LICs performances reported in the previous literature studies.

Anode//Cathode	Voltage range (V)	Energy density (W h/kg)	Power density (W/kg)	Cycling life
$LiTi_2(PO_4)_3$//AC [25]	0-3	14	180	46%@1000 cycles
$LiCrTiO_4$//AC [26]	1-2.5	23	4000	84%@1000 cycles
$Li_2Ti_3O_7$//AC [27]	1-3	20	1000	95%@500 cycles
TiP_2O_7//AC [28]	0-3	13	371	100%@500 cycles
TiO_2//CNT [29]	0-3	12.5	300	83%@5000 cycles
F-Fe_2O_3//AC [30]	0-3	28	2500	90%@5000 cycles
V_2O_5//AC [31]	0-2.7	40	210	80%@10000cycles
T-Nb_2O_5//AC [34]	0.5-2.5	53.79	294	73%@1000 cycles
TiS_2//AC [44]	0-2.6	49	100	76%@2000 cycles
$CNF_@CoNi_2S_4$//AC [48]	1-4	85.4	150	96%@5000 cycles
$TiSe_{0.6}S_{1.4}$//AC [49]	0-2.6	85.4	150	96%@5000 cycles
This work	1-4.2	125.24-60	160-6400	81.75%@40000 cycles

Figure Captions

Figure 1 (a) XRD patterns of CoS, (b) EDS spectra for CoS, (c) XPS spectra (d) Co 2p (e) S 2p spectra for CoS.

Figure 2 (a-c) SEM images for CoS, (d-f) TEM images for CoS, (g) HR-TEM image for CoS, (h) STEM image, together with the related elemental mapping images for CoS.

Figure 3 (a) Galvanostatic charge-discharge patterns for the CoS electrode when the specific current was 0.1 A/g, (b) Coulombic efficiency and cycle performance for the CoS electrode after 300 cycles when the specific current was 0.1 A/g, (c) Galvanostatic charge-discharge patterns for the CoS electrode under various specific currents, (d) Rate performance of CoS electrode under different rates (range, 0.1-5 A/g), (e) The CV curves obtained at different scanning rates (0.1-2 mV/s), (f) b-value determined based on the association of scanning rate with the peak current, (g) Contribution rate of two behaviors at 0.8 mV/s of the CoS electrode, (h) Contribution degree for the diffusion-controlled and capacitive charge versus the scanning rate, (i) Nyquist plots of CoS electrode, the inset is equivalent circuit model.

Figure 4 (a) SEM image for FCS, (b) N2 desorption–adsorption isotherms, (c) Plots showing the distribution of pore size of FCS, (d) The CV curves of FCS under various scanning rates, (e) Cycle performance for FCS when the specific current was 0.1 A/g, (f) Galvanostatic charge-discharge profiles contrasts for FCS as well as AC under at 0.1 A/g, (g) Rate performance for FCS electrode, (h) galvanostatic charge-discharge patterns for the FCS electrode under various current densities, (i) Nyquist plots of FCS electrode, the inset is equivalent circuit model.

Figure 5 (a) Schematic diagram for LIC on the basis of CoS electrode and FCS electrode, (b) The CV curves for CoS//FCS under different scanning rates (range, 2-20 mV/s), (c) Rate performance of CoS//FCS LIC under various densities of current, (d) The galvanostatic discharge-charge curves for CoS//FCS LIC under various densities of current, (e) electrochemical impedance spectra of CoS//FCS LIC recorded as fresh cell and after 40000 cycles, (f) equivalent circuit model of CoS//FCS LIC, (g) Cycling performance of CoS//FCS LIC, (h) The Ragone plots for CoS//FCS LIC, and those scattered points were consistent with LICs data obtained based on related literature.

Table of Contents

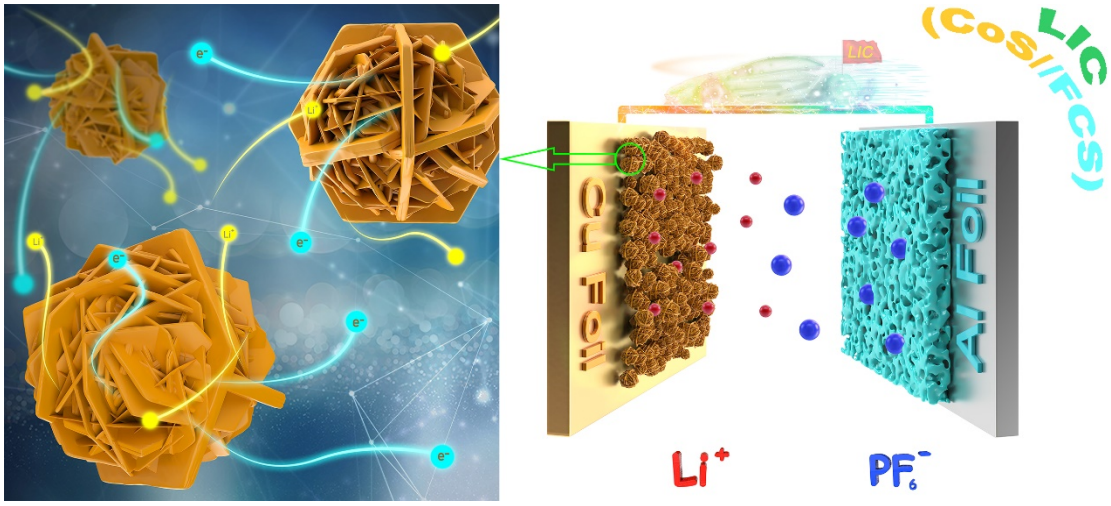

SUPPORTING INFORMATION

3D Hierarchically Structured CoS Nanosheets: Li^+ Storage Mechanism and Application of the High-Performance Lithium-Ion Capacitors

Yun-Kai Wang[a], Mao-Cheng Liu[b], Jianyun Cao[c], Hu-Jun Zhang[a], Ling-Bin Kong* [a, b], David P. Trudgeon[d], Xiaohong Li[d], Frank C. Walsh[e]

[a] State Key Laboratory of Advanced Processing and Recycling of Non-ferrous Metals, Lanzhou University of Technology, Lanzhou 730050, China

[b] School of Materials Science and Engineering, Lanzhou University of Technology, Lanzhou 730050, China

[c] School of Materials, University of Manchester, Oxford Road, Manchester, M13 9PL, United Kingdom

[d] Renewable Energy Group, College of Engineering, Mathematics and Physical Sciences, University of Exeter, Penryn Campus, Cornwall TR10 9FE, United Kingdom

[e] Electrochemical Engineering Laboratory, National Centre for Advanced Tribology & Materials Engineering Research Group, University of Southampton, Highfield, Southampton, SO17 1BJ, United Kingdom

* Corresponding Author. Tel.: +86 (0)931 2976579; Fax: +86 (0)931 2976578; E-mail: konglb@lut.edu.cn

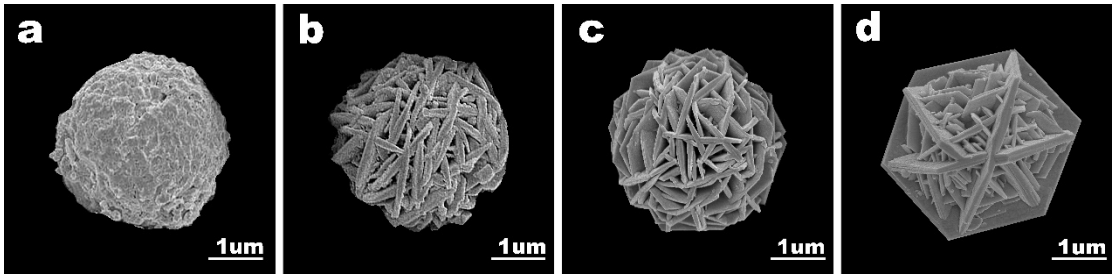

Figure S1 SEM images of the CoS products synthesized from 140 mL of aqueous solution containing 3.75 g mol of CoCl2·6H2O and 6.09 g of thiourea at 200 °C after a given reaction time: (a) 1 h; (b) 4 h; (c) 8 h; and (d) 12 h.

The morphology of samples, which obtained by hydrothermal treatment under different conditions of 1h, 4h, 8h and 12h, were characterized via SEM. After 1 h of reaction, the sample exhibited irregular nanospheres (S1) of about 3 um in diameter aggregated by a number of small CoS nanoparticles. 4 hours later, rough and thick nanosheets were gradually formed on the surface of the microspheres. 8h later, the rough nanosheets become thinner and smoother, and the porous self-assembled microspheres with a morphology of 50-100 nm hexagonal nanosheets interpenetrating each other were formed. As the reaction continues, these anisotropic nanosheets self-assemble through the Ostwald ripening process to form a three-dimensional framework filled with interpenetrating nanosheets (50 nm). During the growth of the crystal, the Ostwald ripening process reduces the binding energy of the entire surface. Finally, a walnut-like 3D Hierarchically Structured CoS was obtained after the reaction reached 12 h. Based on the above experimental results, we speculate that the formation mechanism of the walnut-like CoS structure may be the following steps: (1) The nanoparticles aggregate into microspheres, and it is thermodynamically favorable to form larger crystallites during the initial aggregation. (2) formation and growth of nanosheets on the surface of the microspheres. During this process, the Co2+ and S2- in the solution are preferentially transferred to the surface and formed nucleation spontaneously since the rough surface of the microspheres provides many high energy sites for the nucleation of CoS nanosheets. Furthermore, these differently oriented nanosheets are self-assembled into interpenetrating structures due to its high intrinsic anisotropy. (3) A walnut-like 3D Hierarchically Structured CoS Nanosheets formed Self-assembly by the Ostwald ripening mechanism.

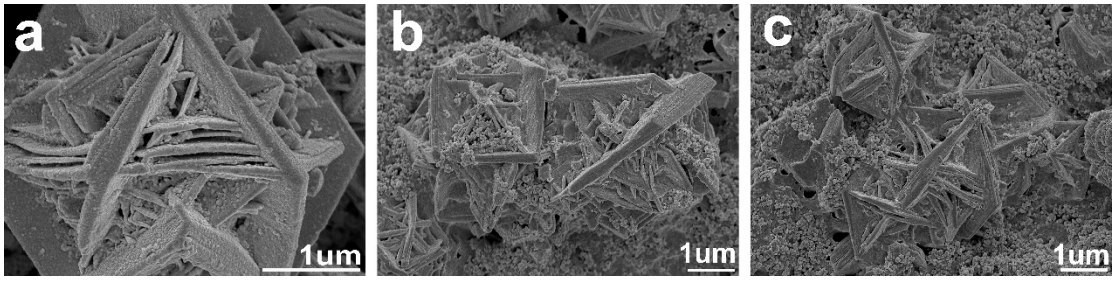

Figure S2 (a) SEM characterization of CoS after 300 cycles of half battery, (b) and (c) SEM characterization of CoS after 10000 cycles of CoS//FCS lithium ion capacitors

The CoS prepared in this paper has excellent structural stability mainly for the following reasons: First, sulfides have better electrical conductivity than other materials. More importantly, the three-dimensional layered structure can well buffer the volume change during the charge and discharge process, and the pores existing between the intersecting nanosheets are beneficial to the diffusion of electrolyte and the transport of lithium ions. In order to verify the above viewpoint,

the morphology of the CoS material after cycling was characterized by SEM. As shown in Figure S2, there is a little of change in the morphology and structure of samples, which indicates that the synthesized CoS material has good structural stability.

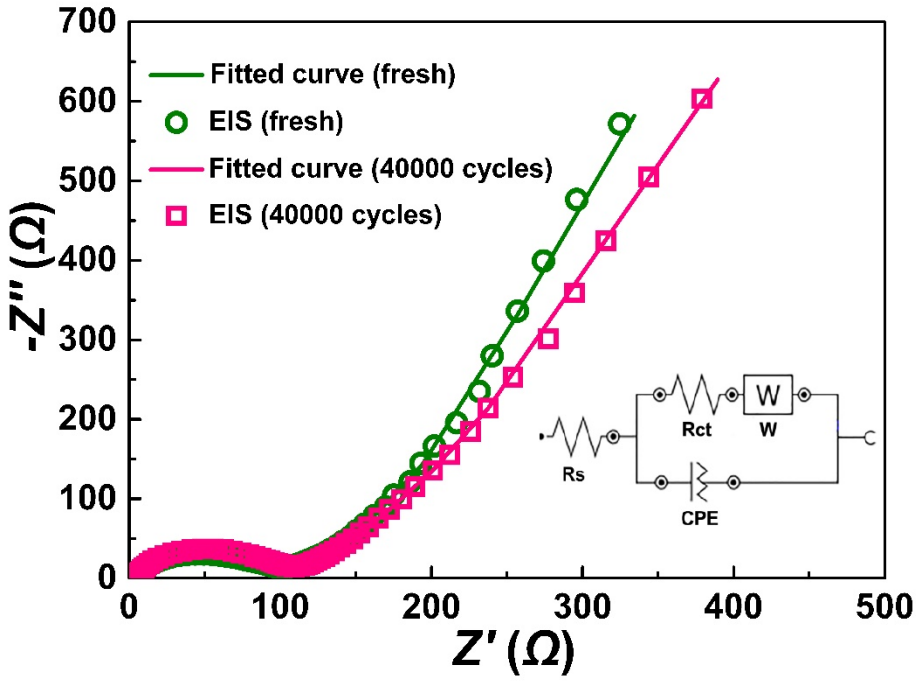

Figure S3 EIS fitting details CoS//FCS lithium ion capacitor before and after cycle

References

(1) Wang, Q., Jiao, L., Du, H., Yang, J., Huan, Q., Peng, W., Yuan, H. Facile synthesis and superior supercapacitor performances of three-dimensional cobalt sulfide hierarchitectures. CrystEngComm, 2011,13(23), 6960-6963.

(2) Lin, W., Huang, Y., He, G. Unique CoS hierarchitectures for high-performance lithium ion batteries. CrystEngComm, 2018,20(42), 6727-6732.

(3) Forghani, M., Donne, S. W. Complications When Differentiating Charge Transfer Processes in Electrochemical Capacitor Materials: Assessment of Cyclic Voltammetry Data. Journal of The Electrochemical Society, 2019,166(8), A1370-A1379.